# Supporting Information

## Enhanced Photocatalytic Degradation of Pollutants via $MoS_2$-Integrated $DyCrO_3$ Nanostructures†

**Md. Mahbubar Rahman, Md. Sobuj Hossain, Tasnim Jahan and M. A. Basith***

## Synthesis of $DyCrO_3$-$MoS_2$ nanocomposites

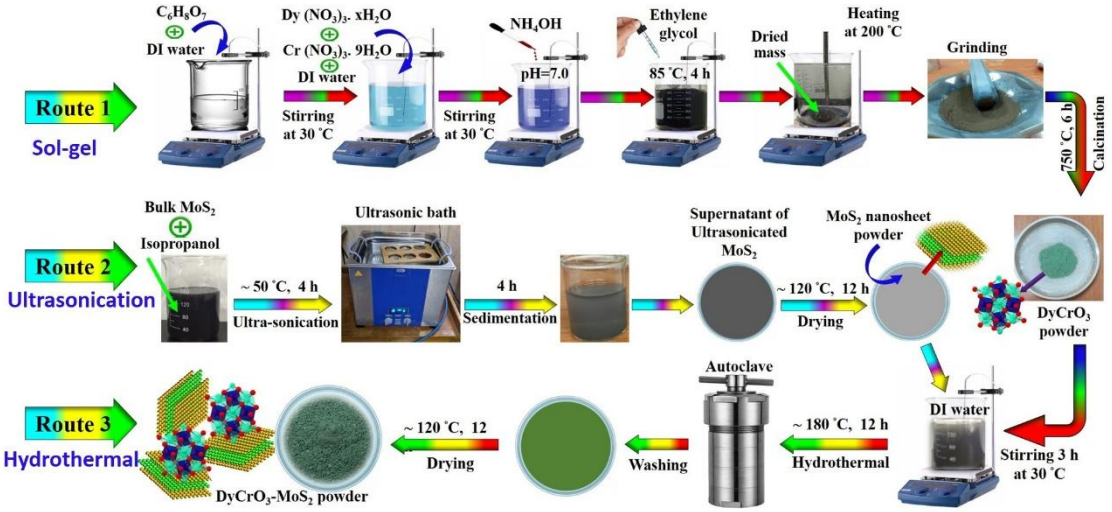


**Fig. S1**. Schematic representation of the synthesis steps of $DyCrO_3$-$MoS_2$ nanocomposites.

## Synthesis of $MoS_2$ Nanosheets

$MoS_2$ nanosheets were synthesized via a liquid-phase exfoliation method assisted by ultrasonication, using commercial bulk $MoS_2$ powder as the starting material [1]. Specifically, 500 mg of $MoS_2$ was dispersed in 100 mL of isopropanol and subjected to bath ultrasonication at 50 °C for 4 h to promote exfoliation. Following sonication, the dispersion was left undisturbed for 4 h to allow the sedimentation of unexfoliated bulk material and thicker layers. The resultant supernatant, enriched with exfoliated $MoS_2$ nanosheets, was decanted and subsequently dried in a hot air oven at 120 °C for 12 h to obtain the final $MoS_2$ NS powder.

## Electrochemical cell setup for Mott-Schottky and Photoelectrochemical analysis

Electrochemical measurements were conducted using a conventional three-electrode system with 1M $Na_2SO_4$ aqueous solution as the supporting electrolyte. An Ag/AgCl electrode is immersed in a saturated 3 M KCl solution, and a platinum wire is employed as the reference and counter electrode, respectively. The photoelectrochemical analysis was done by the symmetric two-electrode system with 1M $Na_2SO_4$ aqueous solution The working electrode was prepared by dispersing 20 mg of the $DyCrO_3$–$MoS_2$ (85%:15%) nanocomposite (comprising 90 wt%) with 2.22 mg of polyvinylidene fluoride (PVDF, 10 wt%) as a binder in 200 µL of N-methyl-2-pyrrolidone (NMP). The mixture was ultrasonicated for 2 h to form a homogeneous slurry, which was then uniformly coated onto a graphite rod (surface area: 0.28 $cm^2$). The coated electrode was dried at 100 °C for 12 h to remove the solvent and ensure firm adhesion of the active material. This modified graphite electrode was subsequently utilized as the working electrode for Mott–Schottky and photoelectrochemical measurements.

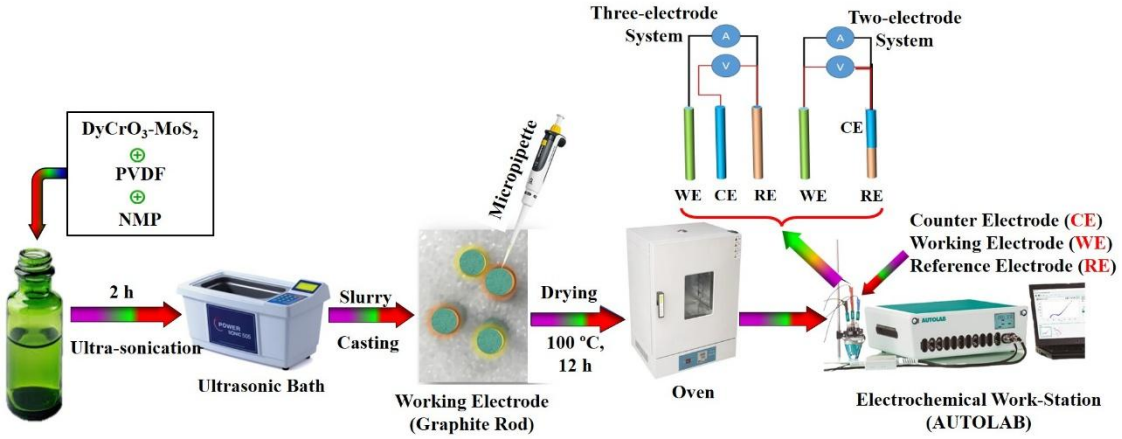


**Fig. S2.** Schematic representation of the preparation of the electrode slurry and the experimental setup for electrochemical measurement.

**Experimental setup for photocatalytic degradation of pollutants from water**

The schematic representation of the photocatalytic reactor setup used for pollutant degradation experiments is shown in Fig. S3. Initially, 1.2 mg of methylene blue (MB) was dissolved in 100 mL of distilled water, and the resulting solution's absorbance spectrum was recorded using a UV–Vis spectrophotometer (UV-2600, Shimadzu, Japan). For the photocatalytic degradation study, 20 mg of $DyCrO_3$–$MoS_2$ nanocomposite was added to 50 mL of the MB solution and stirred in the dark for 1 h to ensure adsorption–desorption equilibrium. The photocatalytic reaction was initiated by irradiating the suspension with a 500 W Hg–Xe lamp (irradiance: 100 mW $cm^{-2}$, simulating solar light). At 30-minute intervals, 6 mL aliquots were collected and centrifuged at 6500 rpm for 3 minutes to remove suspended catalyst particles. The residual concentration of MB was quantified by recording the absorbance spectrum of the supernatant using UV–Vis spectroscopy.

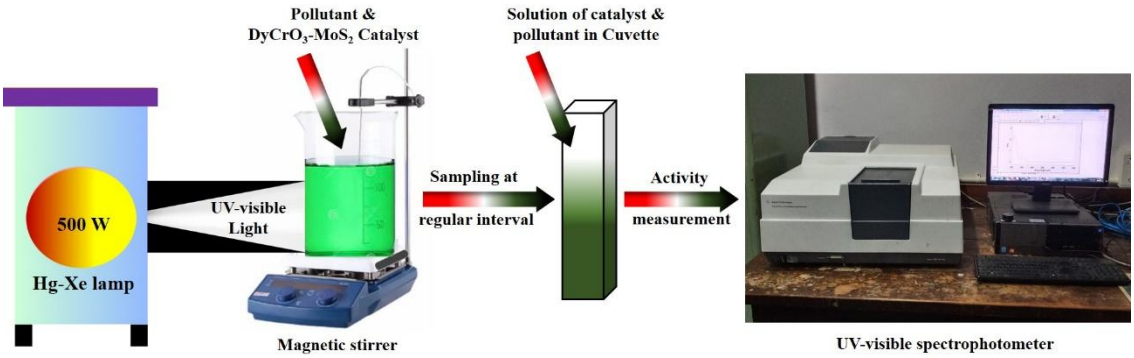


**Fig. S3.** Schematic representation of the experimental setup for photocatalytic degradation of pollutants from wastewater.

Initially, to optimize the catalyst dosage, various amounts (5, 10, 20, and 40 mg) of $DyCrO_3$–$MoS_2$ (80%: 20%) nanocomposite were tested for the degradation of levofloxacin (LFX). Using the optimized dosage, further experiments were conducted to

investigate the effect of $MoS_2$ content (5, 10, 15, and 20 wt%) in $DyCrO_3$–$MoS_2$ nanocomposites on the photocatalytic degradation efficiency for both MB and LFX under identical conditions.

Finally, to evaluate the photocatalytic performance, 10 mg of the optimized $DyCrO_3$–$MoS_2$ (85:15 wt%) nanocomposite was dispersed in 50 mL of MB solution (1.2 mg/100 mL) and irradiated under simulated solar light for 240 minutes. An identical procedure was followed for the degradation of levofloxacin (LFX). The photocatalytic activity was monitored by measuring the UV–Vis absorbance of MB and LFX at their respective maximum absorption wavelengths of 663 nm and 290 nm.

To investigate the photocatalytic mechanism, active species trapping experiments were carried out under solar illumination using selective scavengers. Isopropanol (IPA) was employed to quench hydroxyl radicals ($OH^{\bullet}$), acrylamide for superoxide radicals ($\cdot O_2^-$), silver nitrate ($AgNO_3$) for electrons ($e^-$), and disodium ethylenediaminetetraacetate (EDTA-2Na) for holes ($h^+$). Each scavenger was introduced into the reaction mixture at a concentration of 1.5 mM, and the degradation efficiency was assessed to identify the dominant reactive species involved.

For activation energy analysis, 1 mg of LFX was dissolved in 100 mL of distilled water, and 10 mg of $DyCrO_3$–$MoS_2$ (85:15 wt%) nanocomposite was added to 50 mL of this solution. After stirring in the dark for 1 h to establish adsorption–desorption equilibrium, the mixture was exposed to simulated solar irradiation. Absorbance spectra were recorded after 30 minutes of irradiation at different temperatures (10, 30, and 50 °C). A control experiment was also conducted under identical conditions without the photocatalyst to assess thermal effects in the absence of photocatalysis.

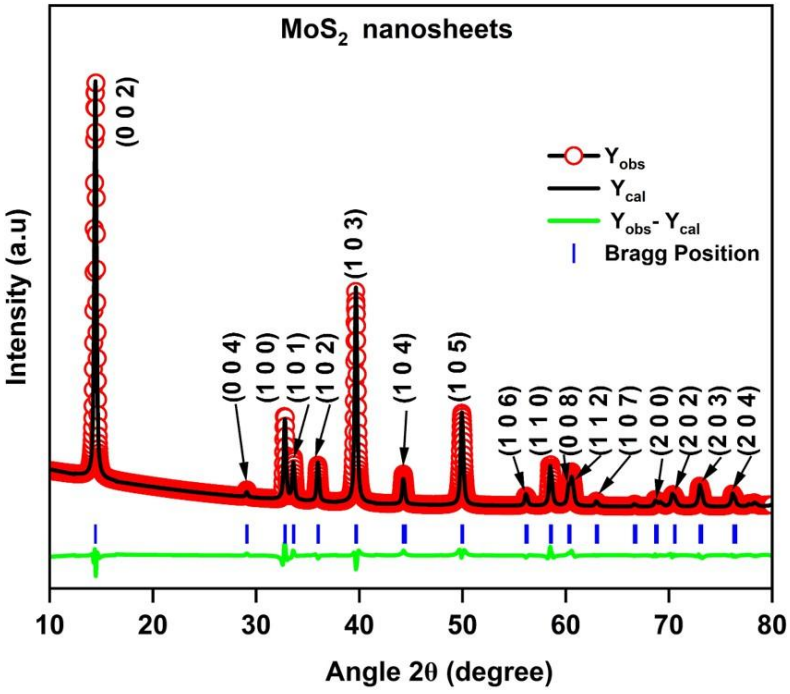

**Fig. S4** The Rietveld-refined XRD profile of pure $MoS_2$ nanosheets exhibits sharper diffraction peaks, with the (0 0 2) reflection at 14.436° showing the highest intensity.

**Crystallite size calculation of $DyCrO_3$-$MoS_2$ nanocomposites:**

The crystallite size was calculated using the Scherrer equation [2], which relates the XRD peak broadening to the dimensions of crystalline domains. The equation is given as:

$$D = \frac{k\lambda}{\beta Cos\theta}$$

where $D$ denotes the crystallite size, $K$ is the shape factor (typically 0.9), $\lambda$ represents the X-ray wavelength, $\beta$ corresponds to the full width at half maximum (FWHM) of the diffraction peak, and $\theta$ is the Bragg angle.

**Table S1.** Crystallographic parameters of $MoS_2$ nanosheets and various concentrations of $MoS_2$ incorporated into $DyCrO_3$–$MoS_2$ nanocomposites, obtained from Rietveld refinement of XRD spectra.

| Sample | $MoS_2$ | $DyCrO_3$:$MoS_2$ (95%:05%) | | $DyCrO_3$:$MoS_2$ (90%:10%) | | $DyCrO_3$:$MoS_2$ (85%:15%) | | $DyCrO_3$:$MoS_2$ (80%:20%) | |
|---|---|---|---|---|---|---|---|---|---|
| Constituents | $MoS_2$ | $DyCrO_3$ | $MoS_2$ | $DyCrO_3$ | $MoS_2$ | $DyCrO_3$ | $MoS_2$ | $DyCrO_3$ | $MoS_2$ |
| Weight (%) | 100 | 95 | 5 | 90 | 10 | 85 | 15 | 80 | 20 |
| Crystallographic phase | Hexagonal | Orthorhombic | Hexagonal | Orthorhombic | Hexagonal | Orthorhombic | Hexagonal | Orthorhombic | Hexagonal |
| Space group | P63/mmc | Pnma | P63/mmc | Pnma | P63/mmc | Pnma | P63/mmc | Pnma | P63/mmc |
| a (Å) | 3.1533 | 5.2637 | 3.15337 | 5.2675 | 3.1533 | 5.2657 | 3.1533 | 5.2710 | 3.1533 |
| b (Å) | 3.1533 | 5.5218 | 3.15337 | 5.5200 | 3.1533 | 5.5198 | 3.1533 | 5.5250 | 3.1533 |
| c (Å) | 12.274 | 7.5445 | 12.2748 | 7.5498 | 12.274 | 7.5509 | 12.274 | 7.5610 | 12.274 |
| $\chi^2$ | 2.5 | 3.5 | | 4.5 | | 2.9 | | 3.5 | |
| Ccrystallite size (nm) | … | 17.05 | | 19.28 | | 22.88 | | 21.23 | |
| Particle size (nm) | … | 28.68 | … | 30.91 | … | 32.78 | … | 32.40 | … |
| Sheets' thickness of $MoS_2$ (nm) | | | | Crystallite size (nm) after four cycles | | | | | |
| 10.99 | | | | 21.98 | | | | | |

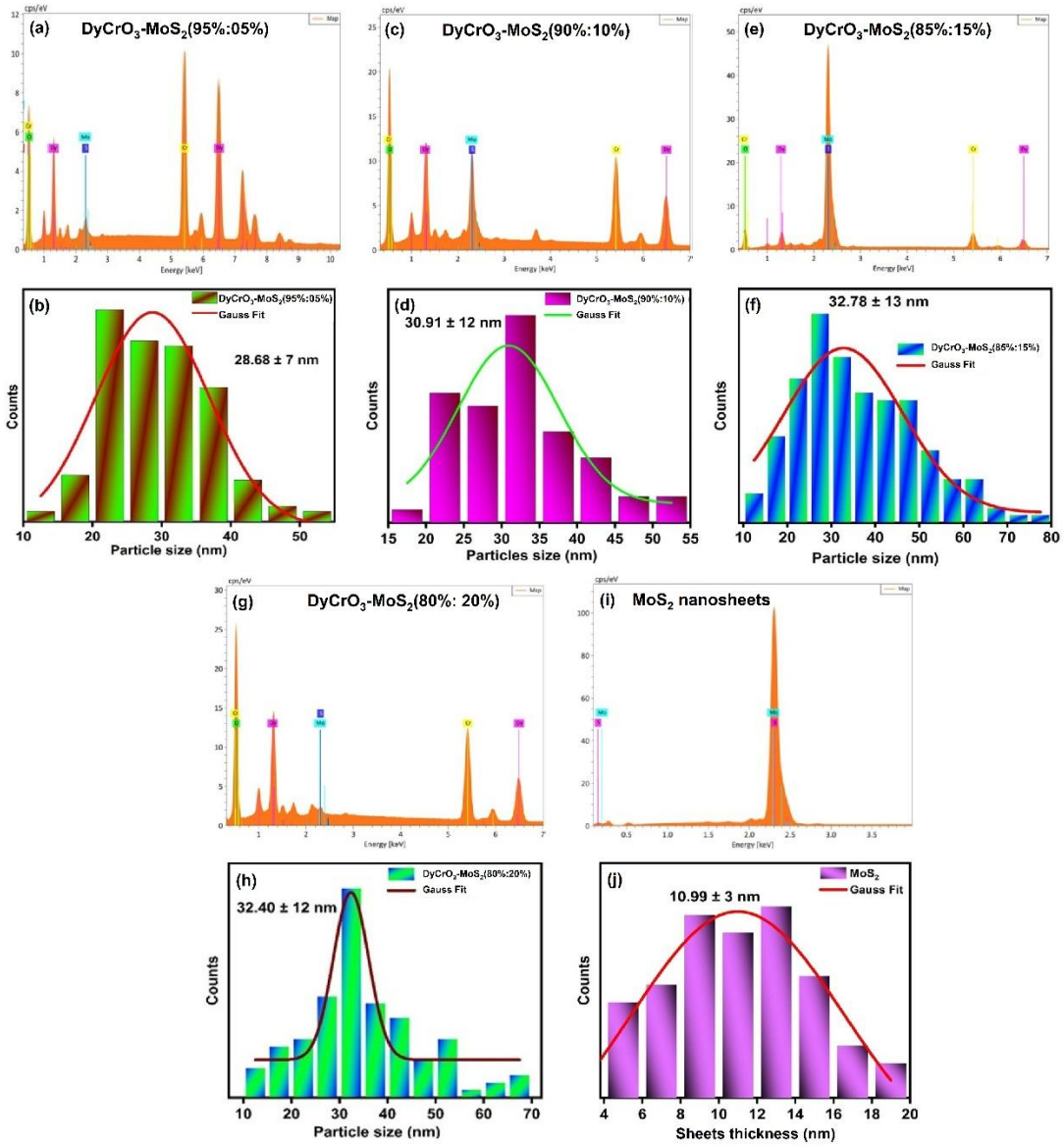


**Fig. S5.** Energy Dispersive X-ray (EDX) spectra and particle size of (a, b) $DyCrO_3$–$MoS_2$ (95%:05%), (c, d) $DyCrO_3$–$MoS_2$ (90%:10%), (e, f) $DyCrO_3$–$MoS_2$ (85%:15%), (g, h) and $DyCrO_3$–$MoS_2$ (80%:20%) nanocomposites, and (i, j) EDX spectra and sheets thickness $MoS_2$ nanosheets.

**Table S2.** Mass and atom percentages of elements in $MoS_2$ nanosheets, and various concentrations of $MoS_2$ incorporated $DyCrO_3$–$MoS_2$ nanocomposites as obtained via EDX and theoretical analysis.

| Sample | Elements | Mass (%) (theoretical) | Mass (%) (experimental) | Atom (%) (theoretical) | Atom (%) (experimental) |
|---|---|---|---|---|---|
| $MoS_2$ | Mo | 59.94 | 59.34 | 33.33 | 32.70 |
| | S | 40.06 | 40.66 | 66.67 | 67.21 |
| $DyCrO_3$–$MoS_2$ (95%:05%) | Dy | 58.81 | 64.40 | 19 | 23.68 |
| | Cr | 18.82 | 19.35 | 19 | 22.23 |
| | O | 17.37 | 13.74 | 57 | 51.30 |
| | Mo | 2.997 | 1.54 | 1.67 | 0.96 |
| | S | 2.003 | 0.98 | 3.33 | 1.82 |
| $DyCrO_3$–$MoS_2$ (90%:10%) | Dy | 55.72 | 50.74 | 18 | 15.41 |
| | Cr | 17.83 | 20.67 | 18 | 19.62 |
| | O | 16.46 | 17.66 | 54 | 54.48 |
| | Mo | 5.994 | 6.19 | 3.33 | 3.19 |
| | S | 4.006 | 4.74 | 6.67 | 7.30 |
| $DyCrO_3$–$MoS_2$ (85%:15%%) | Dy | 52.62 | 17.07 | 17 | 5.01 |
| | Cr | 16.48 | 8.14 | 17 | 7.46 |
| | O | 15.54 | 10.42 | 51 | 31.06 |
| | Mo | 8.990 | 39.62 | 5 | 19.68 |
| | S | 6.01 | 24.75 | 10 | 36.79 |
| $DyCrO_3$–$MoS_2$ (80%:20%) | Dy | 49.53 | 41.76 | 10 | 12.20 |
| | Cr | 15.85 | 18.14 | 16 | 16.57 |
| | O | 14.63 | 17.49 | 48 | 51.92 |
| | Mo | 11.987 | 14.38 | 6.67 | 7.12 |
| | S | 8.013 | 8.23 | 13.33 | 12.18 |

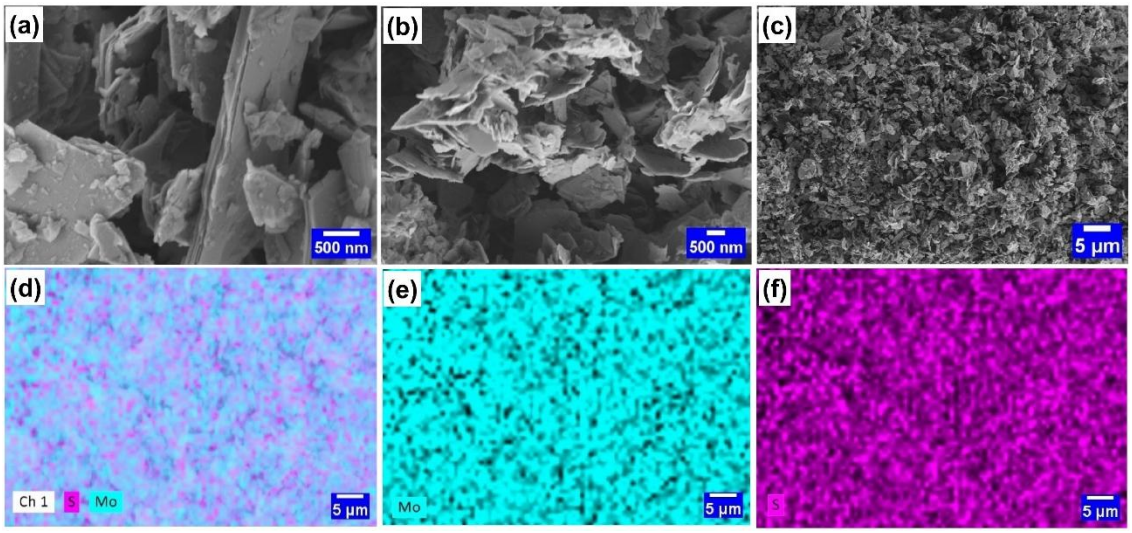


**Fig. S6.** (a) Low-resolution and (b) high-resolution FESEM images of $MoS_2$ nanosheets. (c-f) FESEM micrographs of the synthesized (c) $MoS_2$ nanosheets illustrating (d) the spatial distribution of (e) molybdenum (Mo) and (f) sulfur (S) elements across the nanosheet surface.

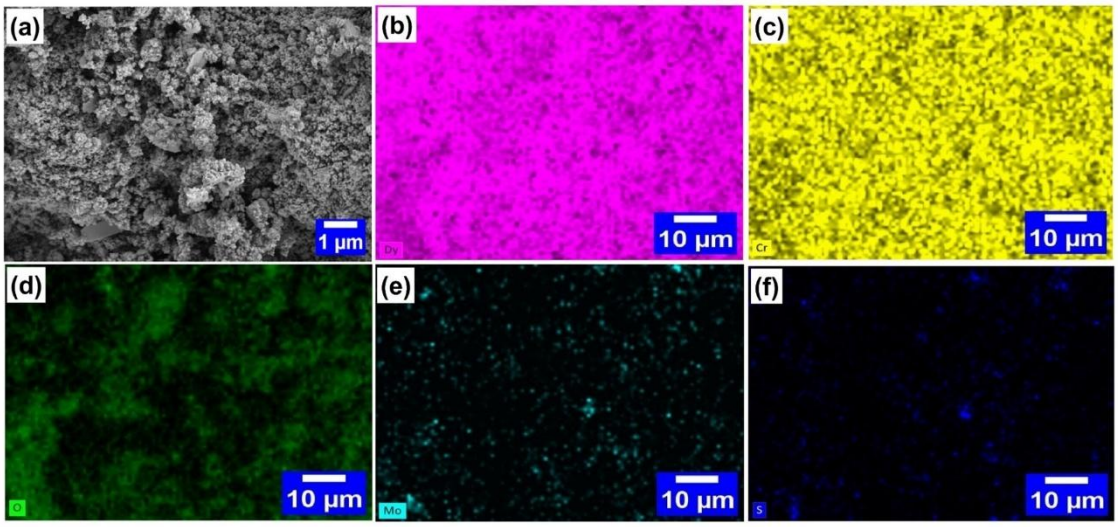


**Fig. S7** (a) FESEM image of the synthesized $DyCrO_3$–$MoS_2$ (95%:05%) nanocomposite. Elemental mapping images confirm the uniform distribution of (b) dysprosium (Dy), (c) chromium (Cr), (d) oxygen (O), (e) molybdenum (Mo), and (f) sulfur (S) throughout the nanocomposite matrix.

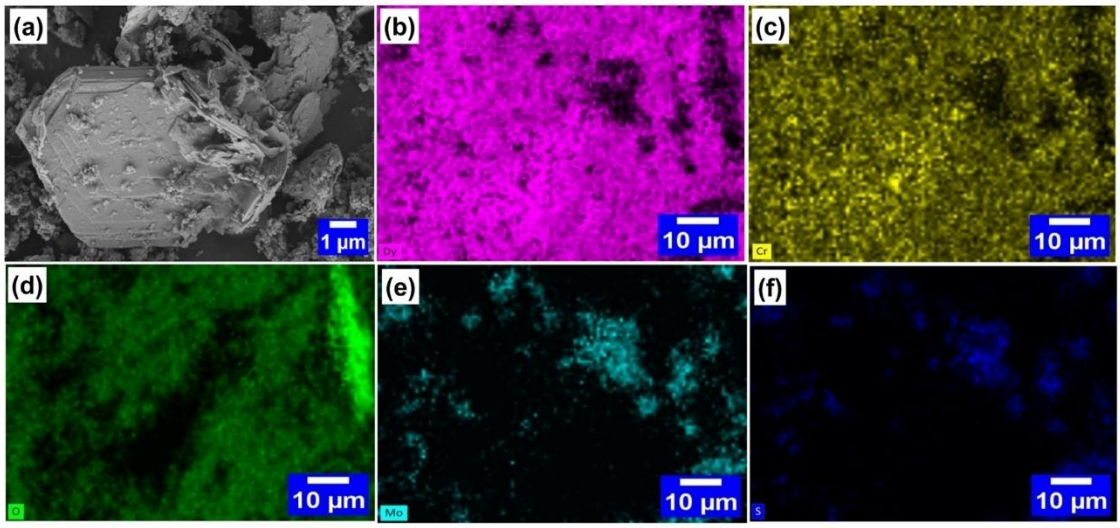


**Fig. S8** (a) FESEM image of the synthesized $DyCrO_3$–$MoS_2$ (90%:10%) nanocomposite. Elemental mapping images confirm the uniform distribution of (b) dysprosium (Dy), (c) chromium (Cr), (d) oxygen (O), (e) molybdenum (Mo), and (f) sulfur (S) throughout the nanocomposite matrix.

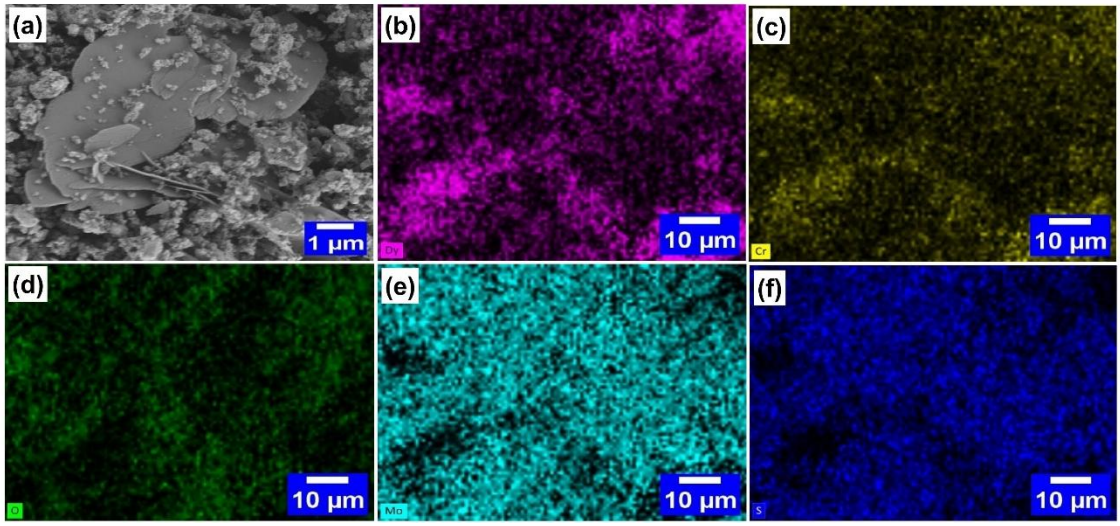


**Fig. S9** (a) FESEM image of the synthesized $DyCrO_3$–$MoS_2$ (85%:15%) nanocomposite. Elemental mapping images confirm the uniform distribution of (b) dysprosium (Dy), (c) chromium (Cr), (d) oxygen (O), (e) molybdenum (Mo), and (f) sulfur (S) throughout the nanocomposite matrix.

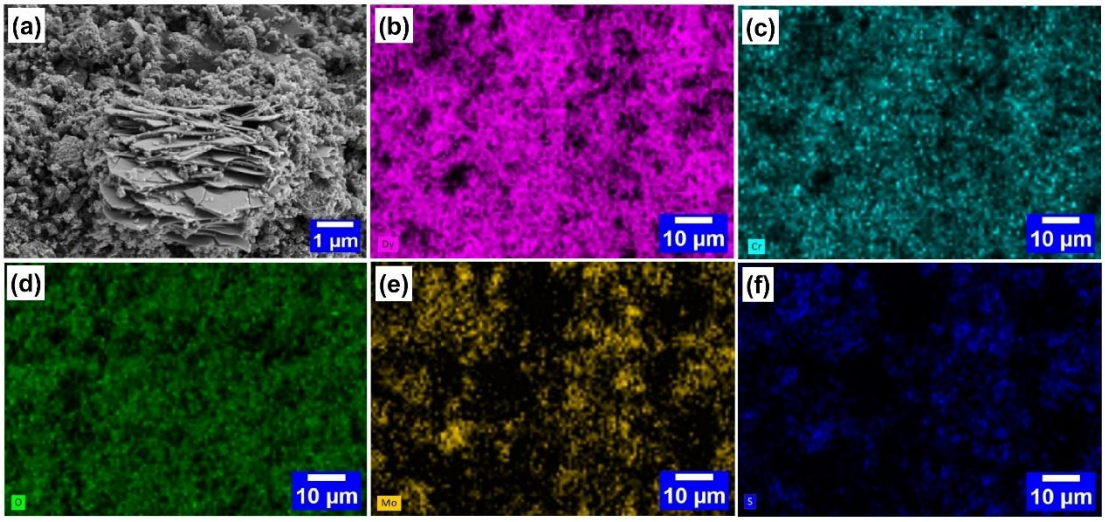


**Fig. S10** (a) FESEM image of the synthesized $DyCrO_3$–$MoS_2$ (80%:20%) nanocomposite. Elemental mapping images confirm the uniform distribution of (b) dysprosium (Dy), (c) chromium (Cr), (d) oxygen (O), (e) molybdenum (Mo), and (f) sulfur (S) throughout the nanocomposite matrix.

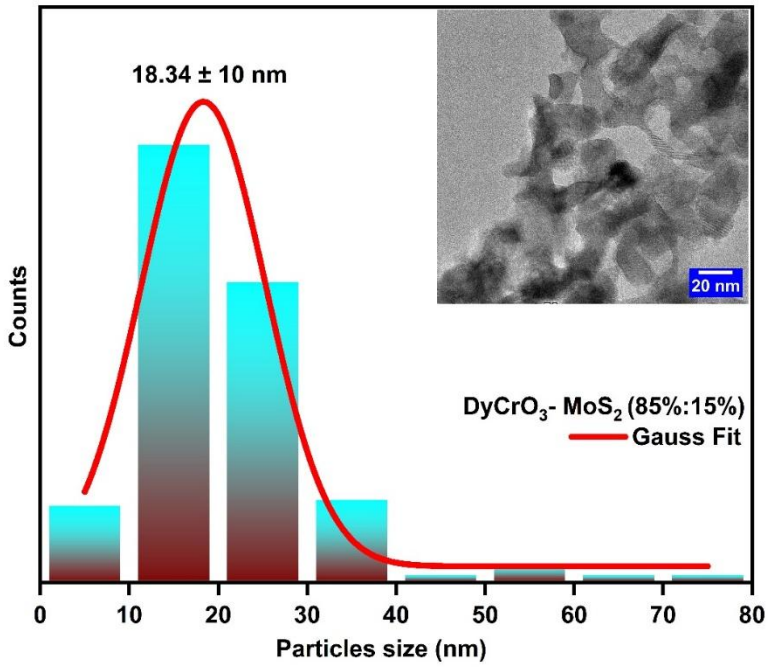


**Fig. S11** (a) Size distribution histogram of $DyCrO_3$–$MoS_2$ (85%:15%) nanocomposite, and the inset indicates the irregular spherical particles from the TEM image of $DyCrO_3$–$MoS_2$ (85%:15%) nanocomposite.

**Table S3.** The XPS spectrum of $DyCrO_3$-$MoS_2$ (85%:15%) nanocomposite revealed several distinct peaks corresponding to the oxidation states of Dy, Cr, O, Mo, and S.

| Element | Orbital | Peaks | Binding energy (eV) |
|---|---|---|---|
| Dy | Dy 4d | Dy $4d_{5/2}$ | 156.16 |
| | | Dy $4d_{3/2}$ | 152.85 |
| | Dy 3d | 3d3/2 ($Dy^{3+}$) | 1334.87 |
| | | 3d5/2 ($Dy^{3+}$) | 1296.77 |
| Cr | Cr 2p | 2p3/2 ($Cr^{2+}$) | 576.47 |
| | | 2p3/2 ($Cr^{3+}$) | 578.06 |
| | | 2p1/2 ($Cr^{2+}$) | 586.35 |
| | | 2p1/2 ($Cr^{3+}$) | 588.26 |
| O | O 1s | $O_{OH}^-$ | 532.00 |
| | | $O_{vcan.}$ | 531.35 |
| | | $O^{2-}$ (metal oxide) | 529.72 |
| Mo | Mo 3d | Mo 3d doublet | 238.53 |
| | | (Mo $3d_{3/2}$) ($Mo^{6+}$) | 235.75 |
| | | (Mo $3d_{5/2}$) ($Mo^{4+}$) | 232.44 |
| | | Mo-S<br>S 2s | 226.63 |
| S | S 2p | $2p_{1/2}$ | 163.37 |
| | | $2p_{3/2}$ | 161.83 |
| | | S–O | 168.97 |

**Band-edge position calculation:**

The band edge positions were experimentally determined using Mott-Schottky analysis [1, 3]. For an n-type semiconductor, the negative x-intercept value, corresponding to the flat band potential ($E_{fb}$) with respect to the Ag/AgCl electrode, was converted into the conduction band minimum ($ECBM$) relative to the NHE electrode using the following equation:

$$ECBM = E_{fb}\ (vs.\ Ag/AgCl) + 0.197 - 0.1\ (V\ vs.NHE)$$

For a p-type semiconductor, the positive x-intercept value, also corresponding to $Efb$ with respect to the Ag/AgCl electrode, was converted into the valence band maximum ($EVBM$) relative to the NHE electrode using the equation:

$$EVBM = E_{fb}\ (vs.\ Ag/AgCl) + 0.197 + 0.1\ (V\ vs.NHE)$$

Subsequently, the value of $EVBM$ for the n-type semiconductor and $ECBM$ for the p-type semiconductor was determined using the following relation: $Eg = EVBM - ECBM$, where $Eg$ represents the optical bandgap, which was obtained from Tauc plots.

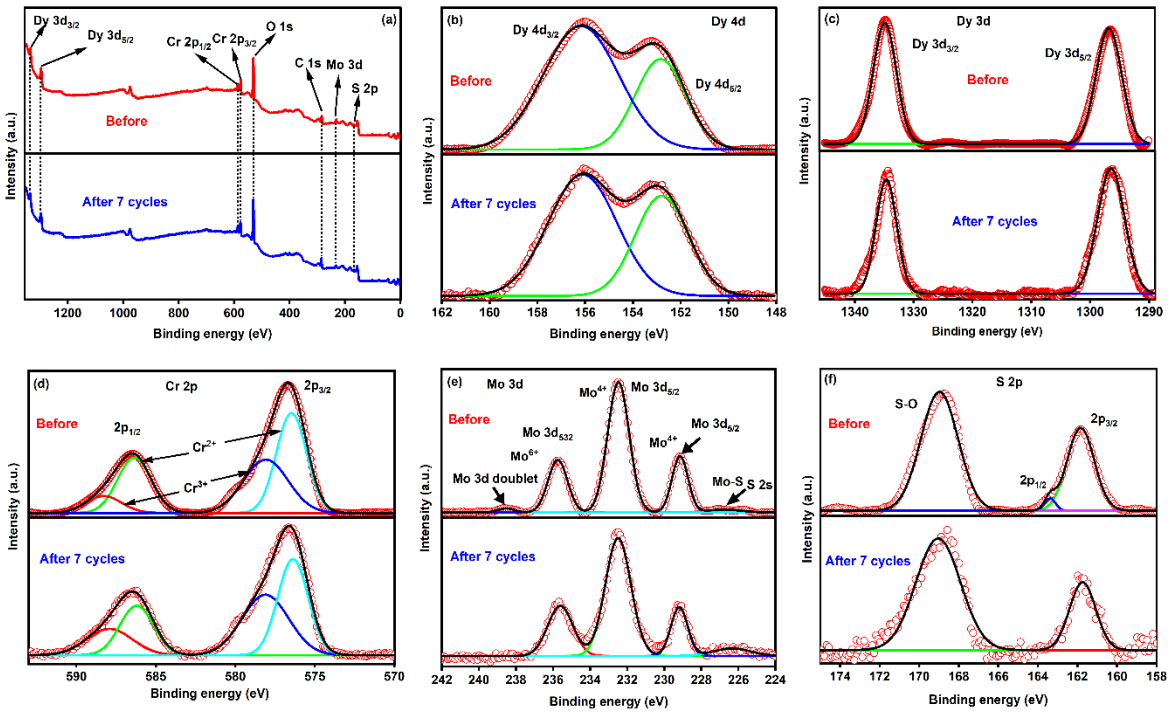


**Fig. S12** XPS spectra of $DyCrO_3$–$MoS_2$ (85:15) before and after seven photocatalytic cycles: (a) survey, (b) Dy 4d, (c) Dy 3d, (d) Cr 2p, (e) Mo 3d, and (f) S 2p regions, showing minor reduction of $Mo^{6+} \rightarrow Mo^{4+}$ and $Cr^{3+} \rightarrow Cr^{2+}$ with preserved surface composition.

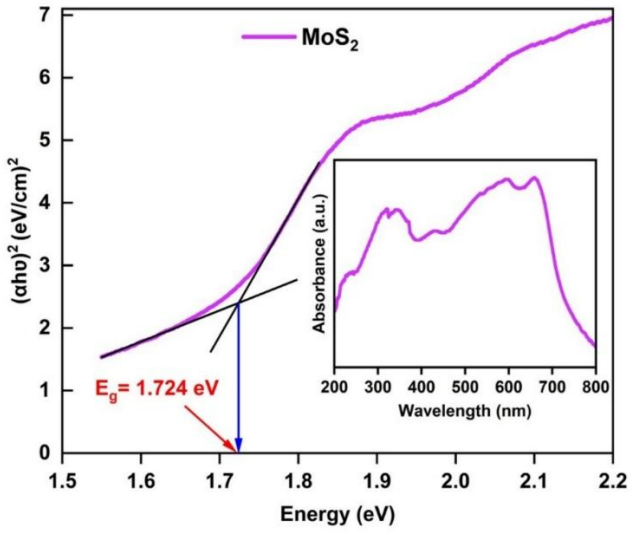


**Fig. S13** The band gap of $MoS_2$ nanosheets and the absorbance spectra are indicated in the inset.

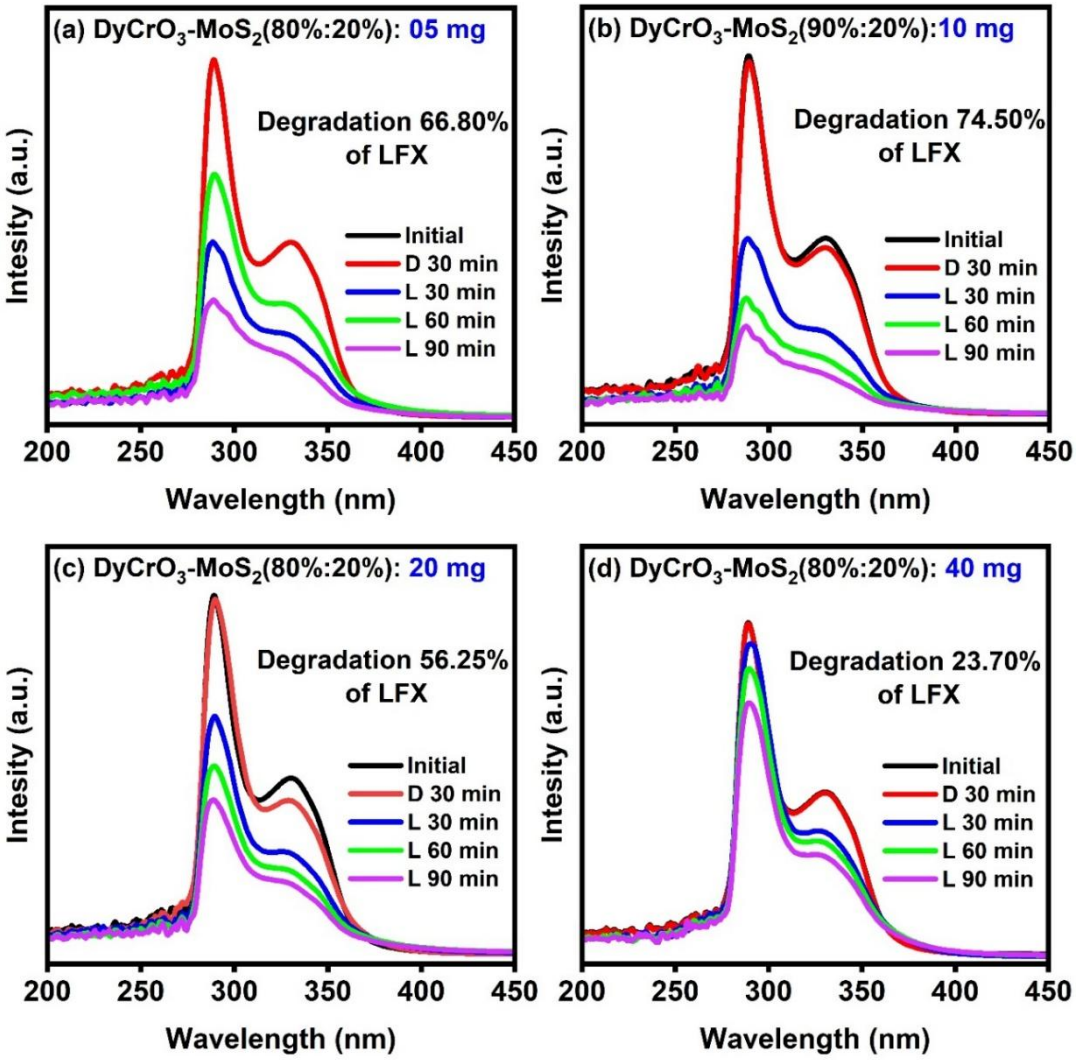


**Fig. S14** The absorbance spectra of LFX for various dosages (5, 10, 20, and 40 mg) of $DyCrO_3$–$MoS_2$ (80%:20%) nanocomposite.

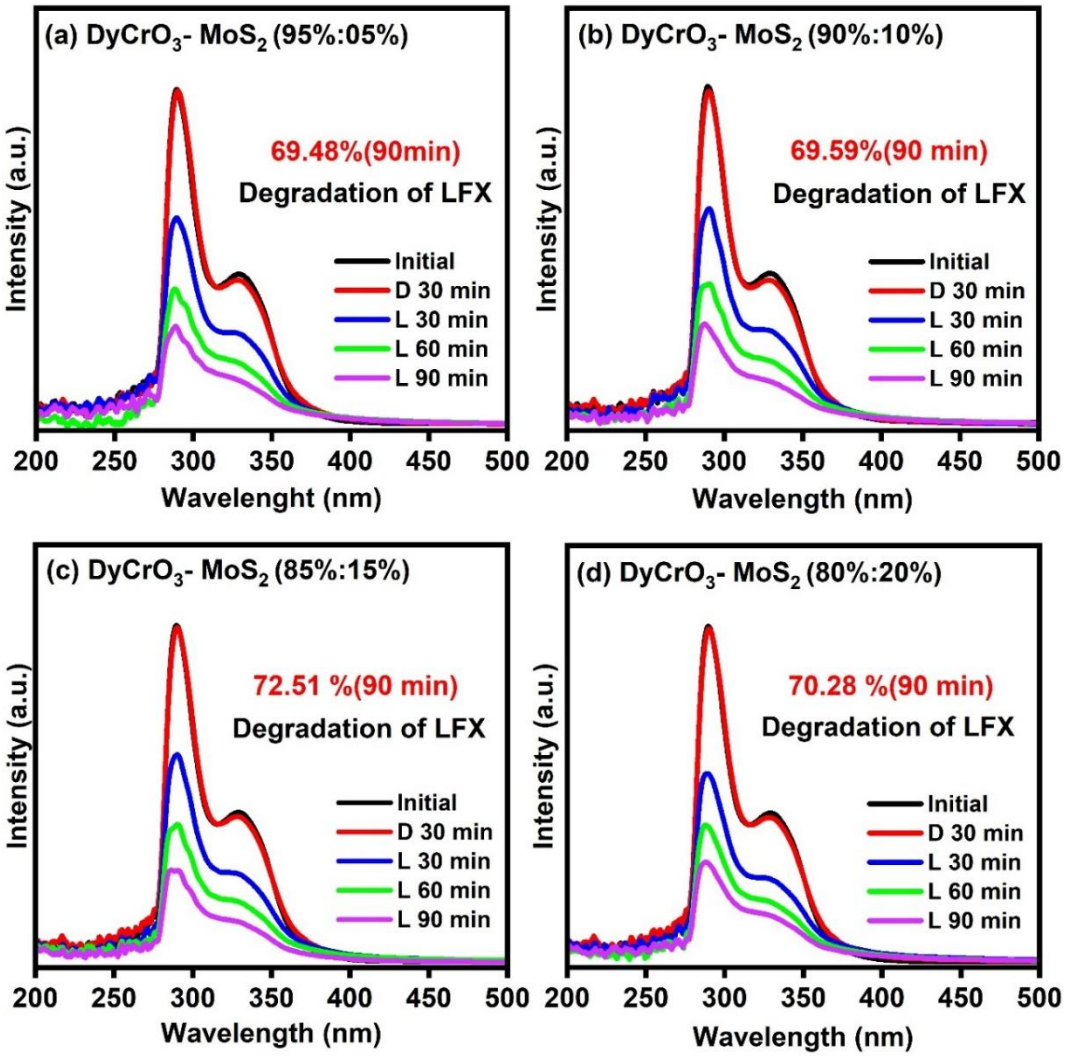


**Fig. S15** The degradation efficiency of LFX under solar irradiation was investigated for 10 mg of different loadings of $MoS_2$.

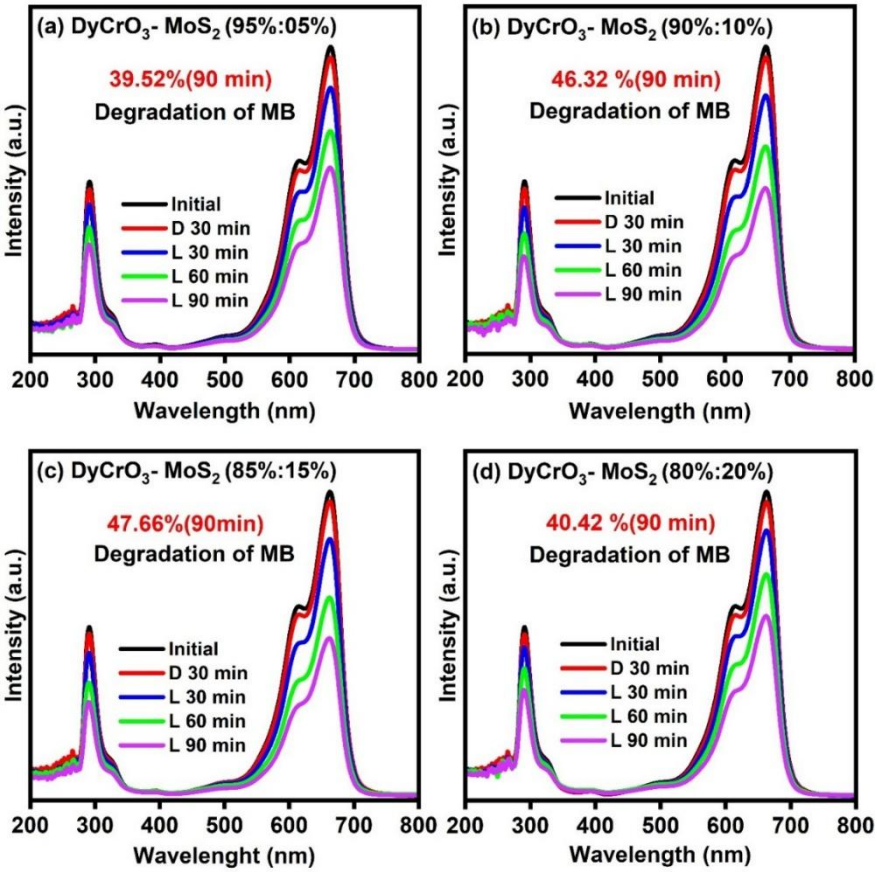


**Fig. S16** The degradation efficiency of MB under solar irradiation was investigated for 10 mg of different loadings of $MoS_2$

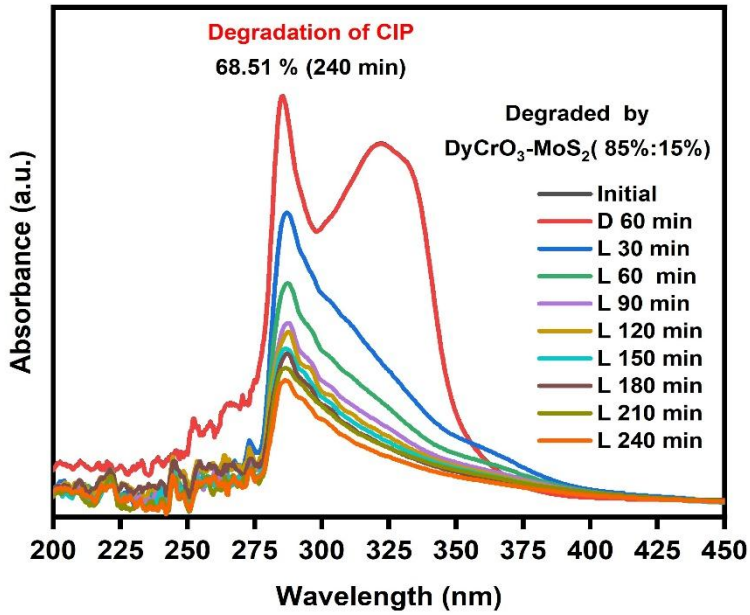


**Figure S17**: Time-dependent UV-Vis spectra for the photocatalytic degradation of CIP by $DyCrO_3$-$MoS_2$ (85%:15%), showing 68.51% degradation in 240 min.

**Apparent quantum yield (AQY)**

**Step 1: Degraded pollutant molecule calculation (240 min)**

| Detail | Unit | $DyCrO_3$–$MoS_2$ (85%:15%) | | |
|---|---|---|---|---|
| | | Degradation of LFX | Degradation of MB | Degradation of CIP |
| Pollutant solution | L | 0.05 | 0.05 | 0.05 |
| Pollutant concentration | g/L | 0.012 | 0.012 | 0.012 |
| Pollutant weight in solution | g | 0.0006 | 0.0006 | 0.0006 |
| Molecular weight | g/mol | 361.368 | 319.85 | 331.346 |
| No. of moles in a solution | mol | $1.6604\times10^{-6}$ | $1.876\times10^{-6}$ | $1.811\times10^{-6}$ |
| No. of molecules in a mole | molecules/ mol | $6.02\times10^{23}$ | $6.02\times10^{23}$ | $6.02\times10^{23}$ |
| Total no. of pollutant molecules | molecules | $9.99\times10^{17}$ | $11.23\times10^{17}$ | $10.9\times10^{17}$ |
| Degradation percentage | % | 84.95 | 78.97 | 68.51 |
| No. of degraded molecules | molecules | $8.486\times10^{17}$ | $8.868\times10^{17}$ | $7.4676\times10^{17}$ |

**Step 2: Photon energy calculation**

Wavelength of light $\lambda = 440$ nm $= 440 \times 10^{-9}$ m

Energy of one photon $E = \frac{hc}{\lambda} = \frac{6.6\times10^{-34}\times3\times10^{8}}{440\times10^{-9}} = 4.50 \times 10^{-19} Joules$

The total energy of light falling per second per unit area is

$E_{Total} = 100\ mW\ cm^{-2} = 100 \times 10^{-3}\times10^{4} W\ m^{-2} = 1000\ W\ m^{-2}$

Number of Photons $= \frac{E_{Total}}{\mathrm{E}} = \frac{1000}{4.50\times10^{-19}} = 2.22 \times 10^{21}$

Area of exposed solution $\frac{2\pi rl}{2} = \pi rl$

Total number of photons falling on the solution (Number of incident photons) = Number of photons × Area of exposed solution

Apparent Quantum Yield (AQY)$= \frac{\text{Number of degraded molecules}}{\text{Number of incident photons}} \times 100$

| Irradiation time (min.) | Area of exposed solution ($m^2$) | Number of incident photons | Apparent Quantum Yield (%) by using ($DyCrO_3$–$MoS_2$ (85%: 15%) nanocomposite | | |
|---|---|---|---|---|---|
| | | | Degradation of LFX | Degradation of MB | Degradation of CIP |
| 240 | 0.001007 | $2.24\times10^{18}$ | 37.88 | 39.59 | 36.21 |

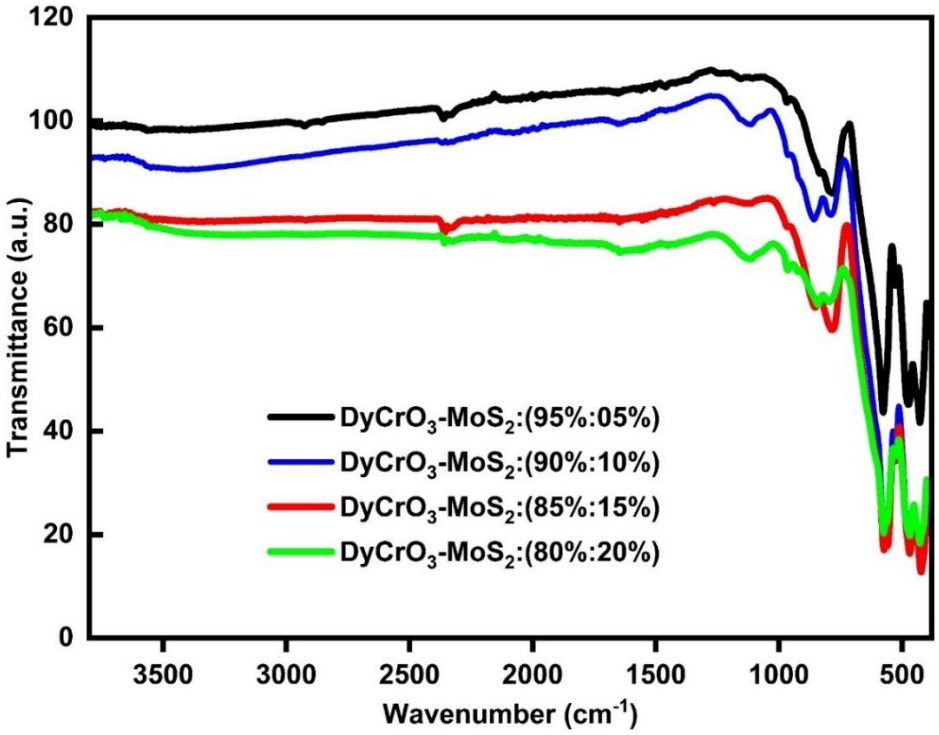


**Fig. S18** FTIR spectra of $DyCrO_3$–$MoS_2$ (95%: 05%), $DyCrO_3$–$MoS_2$ (90%: 10%), $DyCrO_3$–$MoS_2$ (85%: 15%), and $DyCrO_3$–$MoS_2$ (80%: 20%) nanocomposites in the wavenumber range of 4000–400 $cm^{-1}$

Fourier Transform Infrared Spectroscopy (FTIR) analysis was performed using a Shimadzu IRSpirit-T (Japan) to identify the functional groups present in the samples. The measurements were conducted at room temperature within the spectral range of 400–4000 $cm^{-1}$ for $DyCrO_3$ nanoparticles, $DyCrO_3$–$MoS_2$ (85%: 15%) nanocomposites, and $MoS_2$ nanosheets, as depicted in Fig. S18. A broad band observed between 3208–3348 $cm^{-1}$ is attributed to O–H stretching vibrations [3]. The peak near 2340 $cm^{-1}$ is attributed to trace moisture present in the KBr, which was used as the binding medium [4]. In the FTIR spectrum of $MoS_2$, a broad absorption band at 2918 $cm^{-1}$ corresponds to the stretching vibrations of C–H bonds [5]. Additionally, distinct absorption peaks at 2085, 1984, 1430, 1111, and 893 $cm^{-1}$ are identified as the characteristic vibrational modes of $MoS_2$ [6, 7]. The vibrational bands observed near 1735 $cm^{-1}$ and 1640 $cm^{-1}$ are associated with the bending mode of H–O–H [4]. More interestingly, in the DCOMS nanocomposites, the emergence of peaks at 1630 and 920 $cm^{-1}$ correlates with increasing $MoS_2$ content [8]. Additionally, the bands within the 1380–1450 $cm^{-1}$ range are attributed to Cr–O bond vibrations [4]. The absorption peaks at 1108 $cm^{-1}$ and 802 $cm^{-1}$ are attributed to Si–O–Si bonding, corresponding to the symmetric stretching of Si–O and the asymmetric stretching of Si–O–Si, respectively [9]. Additionally, the broadband near 600 $cm^{-1}$ is associated with Mo–S vibrational modes [6,10], while the peak observed around 468 $cm^{-1}$ represents a characteristic Mo–S vibration of $MoS_2$ [10, 11].

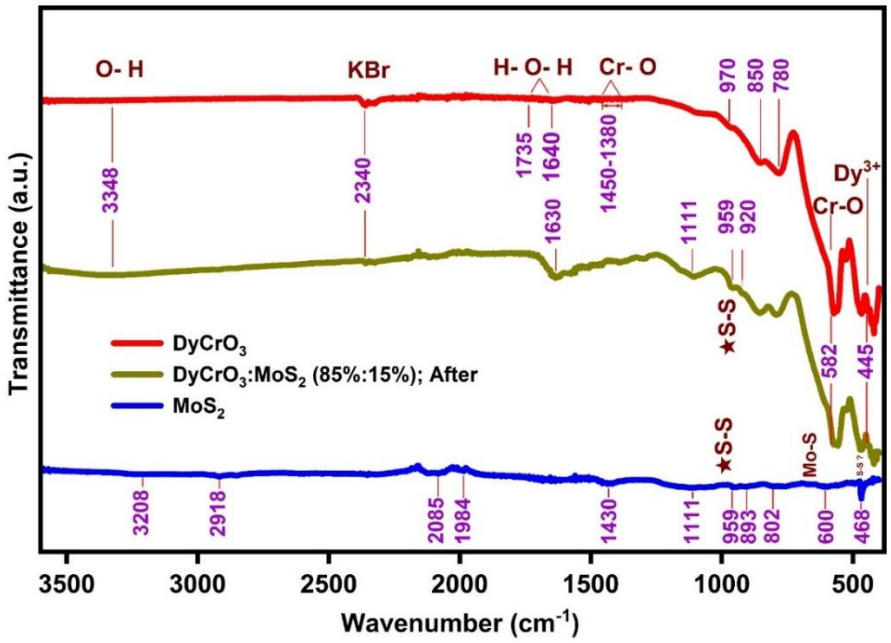


**Fig. S19** FTIR spectra of pristine $DyCrO_3$, $DyCrO_3$–$MoS_2$ (85%: 15%), nanocomposites after four consecutive cycles of degradation, and $MoS_2$ nanosheets in the wavenumber range of 4000–400 $cm^{-1}$.

**References**


[1] M. E. Webber, *Thirst for power: Energy, water, and human survival*, Yale University Press, 2016.

[2] M. Tarek, F. Yasmeen and M. A. Basith, *J. Mater. Chem*. A, 2024, 12, 25475–25490.

[3] H. Maqbool, I. Bibi, Z. Nazeer, F. Majid, S. Ata, Q. Raza, M. Iqbal, Y. Slimani, M.I. Khan, and M. Fatima, *Ceram. Int.*, 2022, *48*(21), pp.31763-31772.

[4] M.M. Rahman, F. Yasmeen, M. Tarek, and M.A. Basith, *J. Alloys Compd.,* 2025, *1010*, p.177295.

[5] S. Ahmad, I. Khan, A. Husain, A. Khan, and A.M. Asiri, 2020, *Polymers*, *12*(12), p.3047.

[6] A. Kaur, S. Rana, A. Bharti, G.R. Chaudhary, and N. Prabhakar, 2021, *Microchim. Acta*, *188*(7), p.222.

[7] K.C. Lalithambika, K. Shanmugapriya, and S.J.A.P.A. Sriram, 2019, *Appl. Phys. A*, *125*, pp.1-8.

[8] S. Acharya, G. Swain, and K. M. Parida, *J. Hydrogen Energy*, 2020, *45*(20), pp.11502-11511.

[9] S.M. Yengejeh, S. Allahyari, and N. Rahemi, *Process Saf. Environ. Prot.,* 2020, 143, pp.25-35.

[10] R. Leelavathi, K. Vivekanandan, and V. Hariharan, 2024, *Acta Phys. Pol. A*, *145*(6).

[11] K.E. Ramohlola, E.I. Iwuoha, M.J. Hato, and K.D. Modibane, 2020, *J. Anal. Methods Chem.*, *2020*(1), p.8896698.

## Data availability statements

The data supporting this article have been included as part of the Supplementary Information.